Paleomagnetic evidence for episodic construction of the Mamiyadake tephra ring

YUKI YASUDA (✉ yasuda@igcl.c.u-tokyo.ac.jp)

The University of Tokyo: Tokyo Daigaku   https://orcid.org/0000-0001-9633-7377

Abstract

Tephra rings that surround maar craters are typically inferred from field observations to be emplaced rapidly over a time period of days to years and thus monogenetic, which is, however, rarely assessed quantitatively. This paper reports the discovery of polygenetic origin of the Mamiyadake tephra ring (Japan), comparing the paleomagnetic directions obtained from throughout the stratigraphy. The new data show that the paleomagnetic directions change systematically with height through the sections, which is interpreted to record paleosecular variation (PSV) of the geomagnetic field during formation of the tephra ring. The paleomagnetic results, together with using an average rate of PSV in Japan, indicate that the Mamiyadake tephra ring was constructed episodically with five major eruptive episodes, separated by centuries or longer, over at least 1000 years. The findings demonstrate that detailed paleomagnetic characterization can uncover the temporal evolution of tephra rings, providing a useful criterion for identifying time breaks, even where field evidence is lacking, and a minimum estimate of the time interval for their emplacement. The approach used here may be applicable to volcanoes of any type.

Introduction

Tephra-ring deposits around maar craters are emplaced during repeated explosive phreatomagmatic explosions (Lorenz 1973; White and Ross 2011; Valentine et al. 2017). They are a few meters to several tens of meters thick and typically consist of coarse-grained lapilli tuffs to tuff breccias interbedded with thinly stratified to cross-stratified tuffs to lapilli tuffs (White and Schmincke 1999; Graettinger and Valentine 2017; Ort et al. 2018). Prehistoric tephra rings are typically inferred to form over a short time span (days to years) due to lack of geological evidence of significant time breaks (Moufti et al. 2013; Valentine and Cortés 2013; Pedrazzi et al. 2014; Agustín-Flores et al. 2015); a few examples show evidence of time gaps as intermittent paleosols, reworked horizons, erosional surfaces, or unconformities (Giaccio et al. 2007; Jordan et al. 2013; Chako Tchamabé et al. 2015). However, such field evidence is qualitative in nature and, in some cases, cannot be seen due to poor exposure.

Paleomagnetic analysis can provide a quantitative means of distinguishing deposits from different eruptions. Paleomagnetic directions preserved in the deposits represent the snapshots of paleosecular variation (PSV) of the geomagnetic field at the time of their deposition. Thus, comparing paleomagnetic directions through the sequence of tephra rings provides a time framework for their emplacement. By using this approach, I present the first high-resolution temporal evolution of a tephra ring (Mamiyadake tephra ring), showing its episodic construction over at least 1000 years.

Ohachidaira Maar-caldera Complex

Ohachidaira volcano is a Quaternary maar-caldera complex with an ~ 2-km-diameter caldera, located in the central part of the Taisetsu volcano group in central Hokkaido, northern Japan (Fig. 1A; Yasuda and Suzuki-Kamata 2018; Yasuda et al. 2020). Early effusive and explosive activities at Ohachidaira volcano emplaced lava flows and pyroclastic rocks, now exposed in the lower half of 100−200 m of the caldera

walls (Fig. 1B), and may have constructed a stratocone (Ishikawa 1963; Konoya et al. 1966). After the cone-building phase ceased, a lithic-block-rich ignimbrite was emplaced on the outer slopes of the cone, forming a crater (Yasuda et al. 2020). The crater was then widened during maar-forming phreatomagmatic eruptions that emplaced the Mamiyadake tephra ring on the crater rim; the northeastern to southeastern parts of the crater may have been further collapsed during a final climactic Plinian eruption (Yasuda et al. 2020). The caldera then filled with water, which is now drained by a creek that dissects the northeastern caldera wall.

Stratigraphy Of The Mamiyadake Tephra Ring

The sequence of the Mamiyadake tephra ring consists of scoria- and lithic-rich phreatomagmatic deposits (massive lapilli tuffs to tuff breccias and stratified to cross-stratified tuffs to lapilli tuffs) interbedded with welded to unconsolidated scoria-fall and ash-fall deposits. On the caldera wall, it is as thick as ~ 90 m and overlies andesitic to dacitic lava flows (Fig. 1B); outside the caldera, it thins rapidly and extends only ~ 1 km downslope. Abundant andesite and dacite lava lithic blocks in the phreatomagmatic units (up to 4 m in size) imply that the shallow part of the conduit was excavated by violent explosions. The northern part of the tephra ring abuts against the southern slope of an older lava dome, and the eastern part of it is overlain by plinian fall deposits of the climactic eruption. No direct age determinations have been made for the Mamiyadake tephra ring; however, the stratigraphic relations and the previously reported ages of the adjacent deposits suggest that it formed sometime between ~ 155 ka and ~ 34 ka (Yasuda et al. 2020).

Paleomagnetic Directions

Paleomagnetic directions were determined at 39 sites in the Mamiyadake tephra ring (Fig. 1A), complementing 8 sites previously reported by Yasuda et al. (2020). Sites were chosen to span as much of the stratigraphy of the tephra ring as possible (Figs. 1B and 1C). The data set includes five successive sites in the north section (N1−5), two in the northwest (NW1−2), nine in the west (W1−9), eight in the southwest (SW1−8), five in the south (S1−5), and eight in the east (E1−8), as well as two isolated sites (I1−2) each southwest and south.

At each site, 6 to 11 samples (8 in average) were collected over 1 to 25 m of outcrop; samples were taken from a bed or beds (up to 3 m thick) of mainly scoria fall and subordinately tuff breccia and lapilli tuff, with only one site from a sintered tuff. All samples (> 5 cm in size) were independently oriented in situ with a magnetic compass and then removed from the outcrop using a rock hammer. To avoid possible orientation error due to strong magnetization of the rock, the deflection of the compass needle was checked while the compass was moved close to and away from the rock before each sampling. Scoria clasts were preferentially sampled (94% of all samples) because (1) they occur throughout the sequence as a major juvenile component and (2) preliminary paleomagnetic data (Yasuda et al. 2015; Yasuda et al. 2020) showed that scoria clasts in this study area tended to yield interpretable results. Lithic samples (andesite and dacite lava blocks and welded lapilli tuff blocks) were subordinate (3%), and only one

pumice clast was sampled. At site NW2, large (> 5 cm) clasts were so rare that sintered bulk-matrix samples were collected instead. Fresh samples were preferentially collected to avoid chemical alternation to remanence. No tilt correction was applied because no field evidence for post-depositional movement of the sampled deposits was observed.

In the laboratory the oriented samples were filled with plaster which were then cored and cut into ~ 24-mm-tall, ~ 25-mm-diameter cylindrical specimens for analysis. Remanence was measured on 313 specimens (one specimen per sample) using a Natsuhara SMM-85 spinner magnetometer. After measurement of the natural remanent magnetization (NRM), all the specimens were thermally demagnetized using Natsuhara TDS-1 thermal demagnetizers with a residual field of < 10 nT. Specimens were heated in 50°C steps between 100°C and 500°C and then in 30°C steps up to 680°C (mostly up to 560–620°C), until the remaining intensity was less than 5% of the NRM or until the magnetization became unstable. Changes in bulk susceptibility with progressive demagnetization were monitored with a Bartington MS2 meter.

Results were plotted on orthogonal vector plots (Zijderveld 1967) and equal-area projections to evaluate the demagnetization behavior (Fig. 2). Principal component analysis (Kirschvink 1980) was used to define the characteristic remanent magnetization (ChRM) of each specimen (see Additional file 1). The magnetic components were considered stable where they were defined by at least three points (not including the origin) on vector plots with a maximum angular deviation (MAD) of < 10. Data were analyzed using the MagePlot programs (Hatakeyama 2018), with the data of Yasuda et al. (2020) reanalyzed following the procedure outlined above.

Most (77%) of the specimens were fully unblocked at temperatures between 530°C and 590°C (Figs. 2A–D), indicating that magnetite is the carrier of the magnetization. Subordinate specimens had higher unblocking temperatures with up to 37% (mostly 5–25%) of the NRM remaining at 590°C and were fully unblocked at 620°C (Fig. 2E), suggesting the presence of minor hematite. Only one scoria specimen from site S4 retained more than 20% of the NRM at temperatures 590–650°C and was fully unblocked at 680°C, the Curie temperature of hematite (Fig. 2F). The magnetite and hematite components had nearly identical directions (Figs. 2E and 2F).

Of the 313 specimens measured, 293 showed a stable component that decayed univectorially to the origin during demagnetization, the direction of which is consistent within each site (see Additional file 1). This component was interpreted as the ChRM. Any overprint component was typically removed by temperatures of 100–400°C (Figs. 2B–F). Eleven specimens were overprinted with magnetizations that were not removed even at the highest demagnetization steps (530–620°C), so they were rejected for further analysis. Their direction during thermal demagnetization gradually changed toward the ChRM direction, but the remanence was completely removed before isolating the ChRM (Fig. 2G). There were also six specimens rejected because they were unstable during demagnetization (Fig. 2H). Three specimens had resolvable characteristic directions but with peculiar directions > 30° from the average of the samples from that site, and they were discarded from site-mean calculations. These divergent

directions are likely due to misorientation during sampling, post-cooling movement of the sampled clasts when deposits were loosely packed, or complete overprinting.

Although within-site dispersions in ChRM are small with α_{95} values ranging from 1.7° to 6.5° (3.3° in average) and k values ranging from ~ 100 to ~ 1100 (~ 400 in average), declinations (337.2°−21.8°) and inclinations (50.1°−75.0°) of the mean directions scatter widely (Table 1).

Most sections show vertical changes in site-mean directions (Fig. 3). Four lines of evidence indicate that the ChRMs represent the primary thermoremanent magnetization acquired when each unit was emplaced and cooled and that the directional changes represent PSV of the geomagnetic field over time: (1) the ChRMs are the stable component carried predominantly by magnetite; (2) the ChRM directions are well grouped within each site, irrespective of any type of specimens (scoria, pumice, lithic, tuff; Table 1); (3) the site-mean ChRM directions disperse up to 16.3° away from the geocentric axial dipole field direction (at latitude 43.7°N, $D = 0°$, $I = 62.4°$), the degree of which is within the expected limits of geomagnetic secular variation in Japan (Hyodo et al. 1993; Hatakeyama 2013); (4) very similar directional variations recorded in the west and southwest sections, as detailed below, indicate that the paleomagnetic methods employed here gave reproducible results and that the variations in paleomagnetic directions are realistic.

Paleomagnetic Stratigraphy

North Section

The North section, ~ 50 m thick, consists predominantly of lithic-rich (dominantly andesite lava blocks up to 4 m) coarse tuff breccias. Sampling was done at five sites, including the lowermost exposed tuff breccia unit (N1) and a scoria-fall unit near the top of the section (N5). Paleomagnetic directions of N1−5 are virtually identical (Fig. 3A) indicating that the section was emplaced rapidly enough that no significant secular variation was recorded.

Western (Southwest, West, and Northwest) Sections

The tephra-ring deposits exposed on the western caldera walls are 50−90 m thick and consist of tuff breccias, stratified to cross-stratified tuffs to lapilli tuffs, and scoria-rich falls. The layers are traceable along the wall from the west section to the southwest section, where they become thinner and finer grained. These two sections show parallel changes in paleomagnetic directions with height (Fig. 3B). The paleomagnetic data demonstrate that there are four major eruptive episodes (1−4) recorded in these sections, with the first one only recorded in the west section. Deposits of eruptive episode 1 include the lowermost exposed tuff breccias (W1) in the west section. The tuff breccias consist of coarse andesite lava blocks (up to 2.7 m) and scoria lapilli, very similar in appearance and composition to those in the north section, and paleomagnetic directions of W1 and N1−5 are nearly identical (Fig. 3B), suggesting that they were erupted during the same eruptive episode.

Deposits of eruptive episode 2 include three sites in the west section (W2–4) and four in the southwest (SW1–4). They yield very similar paleomagnetic directions, which differ significantly from those of eruptive episode 1 (W2–4, SW1–4 vs. N1–5, W1; Fig. 3B). Deposits of eruptive episode 3 include four sites in the west section (W5–8) and three in the southwest (SW5–7), which yield north-northwest paleomagnetic directions that are indistinguishable from each other (Fig. 3B) and from that of an independent site (I1) on the foot of the southwest inner wall (Fig. 3D), suggesting coeval emplacement. Eruptive episode 4 is recorded in the uppermost sites in the west (W9) and southwest (SW8) sections with indistinguishable north-northeast directions (Fig. 3B).

The tephra-ring deposits in the northwest section is probably up to ~ 50 m in thick, of which the upper ~ 20 m is exposed and was sampled at two sites, one (NW2) from a sintered tuff within the topmost unit on the rim and the other (NW1) from a scoria-fall unit below. The vertical change in paleomagnetic directions between NW1 and NW2 is consistent with that between eruptive episodes 2 (W2–4, SW1–4) and 3 (W5–8, SW5–7), implying their correlation (Fig. 3C).

South Section

Five sites (S1–5) were sampled from ~ 50 m of the tephra-ring deposits at the head of the valley to the south of the caldera (Fig. 1C). They include scoria-fall units at the base (S1) and in the upper parts (S4–5) of the section, and tuff breccia (S2) and lapilli tuff (S3) units in the middle of the section. Owing to talus cover, visual stratigraphic correlation cannot be made between the south and southwest sections. Paleomagnetically, S3 and S5 are very similar to the sites of eruptive episodes 2 (e.g., W2–4, SW1–4) and 3 (e.g., W5–8, SW5–7), respectively, suggesting correlation between the sections (Fig. 3D). The direction of S4 is similar to those for eruptive episode 3 but distinguishable from that of S5 and plotted between those of S3 and S5, which possibly suggest a minor eruption that occurred between eruptive episodes 2 and 3. The lowest two sites, S1–2, have directions that are independent of other known directions (Fig. 3D). These directions are similar to but shallower than those for eruptive episode 4 (W9, SW8), and are nearly identical to that of an independent site in the south wall (I2) where samples were collected from a scoria-fall unit near the base. These lower parts of the southern tephra-ring deposits likely record an eruptive episode (informally called eruptive episode X) that is not represented in the data of the other sections. It is probably preceded eruptive episode 2, but the temporal relationship between eruptive episodes X and 1 is unclear.

East Section

The east section, at least 50 m thick, was sampled at eight sites (E1–8), including the lowermost exposed unit of ~ 15-m-thick stratified tuff breccias (E1–2) and the uppermost exposed scoria-fall deposits (E8). All the units sampled yield virtually identical paleomagnetic directions (Fig. 3A) suggesting they were emplaced within a brief time interval. The discontinuity of outcrops prevents field correlation between the east and the other sections, but paleomagnetically the east section is indistinguishable from the sites of eruptive episode 2 (e.g., W2–4, SW1–4; Fig. 3D) suggesting their coeval emplacement.

Paleomagnetic Estimation Of Eruptive Intervals

The time intervals between emplacement of volcanic deposits with different paleomagnetic directions can be estimated using secular variation rates calculated from local paleomagnetic and archaeomagnetic records (McIntosh et al. 1992; Chenet et al. 2008; Jarboe et al. 2008). The archaeomagnetic data that cover the last 1600 years in Japan (Hatakeyama 2013) indicate an average secular variation rate of 6° per century (ranging from 1° to 14°); the same average rate has been estimated from data obtained from the sedimentary rocks in Japan that span 500–11,650 year BP (Hyodo et al. 1993). There are periods when the rates are very low (< 2° per century), but they typically last a century or less. These data suggest that a time break of a century or more can be reflected in the deposits by distinguishable paleomagnetic directions.

The Mamiyadake tephra ring records 5 distinct eruptive episodes, each corresponding to discrete clusters of the site-mean paleomagnetic directions. The angular distances between episode-mean directions range from 10.4° to 20.2°; in total, the field direction must have moved at least 65.9° during the eruptions (Fig. 4). Assuming that the geomagnetic field during formation of the Mamiyadake tephra ring changed similarly to that during the Holocene and using an average variation rate of 6° per century, the data suggest that the tephra ring formed over at least ~ 1000 years with four major breaks of a few hundred years or longer. These duration estimates are minimum values, because the true paths of the field are likely more complex, deviating from a straight line between each pair of episode-mean directions (Fig. 4).

Field Evidence For Eruptive Hiatus

Paleosols and unconformities represent significant time breaks in the volcanic stratigraphy (e.g., Lucchi 2019). No paleosols, however, are observed within the sequence of the Mamiyadake tephra ring, likely due to alpine environments above the tree line (~ 1500 m above sea level) that are unfavorable for the development of soil as is the case for this area today. Three clear angular unconformities were found in the sequence, one between sites NW1 and NW2, one between sites W8 and W9, and the other between sites SW6–7 and SW8 (Fig. 1B). The first one is correlated with the boundary of eruptive episodes 2 and 3, while the other two are correlated with that of eruptive episodes 3 and 4. These unconformities must have developed during eruptive hiatus due to aeolian erosion.

Time breaks in the Mamiyadake sequence are not always accompanied by field evidence. At the south section, no clear unconformity or major reworked deposits can be observed within the deposits (Fig. 1C). Such a field observation alone would suggest a rapid (days to years) emplacement of the section; the paleomagnetic data, however, demonstrate that there are two (or possibly three) significant breaks of a century or longer. The results suggest that there may be time breaks missed in the volcanic record, and such breaks are likely to be identified using paleomagnetic directions. More accurate identification of time breaks should lead to more accurate estimations of the frequency and magnitude of eruptions, thus improving hazard mitigation.

Comparison To Other Maar Tephra Rings

Maar tephra rings typically show no field evidence of major breaks in activity and are thus considered to be monogenetic (Németh and Kereszturi 2015). The episodic and long-term (> 1000 years) evolution of the Mamiyadake tephra ring is unusual but not the only example. Freda et al. (2006) revealed by $^{40}Ar/^{39}Ar$ dating that the Albano maar formed during three major eruptive episodes at ~ 69, 39, and 36 ka. Even longer timespan for formation of the Barombi Mbo maar was reported, by K-Ar dating, in that it formed during three eruptive cycles that span ~ 430,000 years (Chako Tchamabé et al. 2014). These examples clearly indicate that a longer-term (> 1000 years) perspective should be considered for hazard assessment of such volcanoes (Lorenz 2007).

Abbreviations

PSV: Paleosecular variation; NRM: Natural remanent magnetization; ChRM: Characteristic remanent magnetization; MAD: Maximum angular deviation; D: Declination; I: Inclination; EP: Eruptive episode.

Declarations

Ethics approval and consent to participate

Not applicable.

Consent for publication

Not applicable.

Availability of data and materials

All data generated or analyzed during this study are included in this published article and its supplementary information file.

Competing interests

The author declares that there is no conflict of interest.

Authors' information

YY is a postdoc at Research Center for Advanced Science and Technology, The University of Tokyo.

References

1. Agustín-Flores J, Németh K, Cronin SJ, Lindsay JM, Kereszturi G (2015) Shallow-seated explosions in the construction of the Motukorea tuff ring (Auckland, New Zealand): Evidence from lithic and sedimentary characteristics. J Volcanol Geotherm Res 304:272–286. https://doi.org/10.1016/j.jvolgeores.2015.09.013

2. Chako Tchamabé B, Ohba T, Issa, Ooki S, Youmen D, Owona S, Tanyileke G, Hell JV (2014) Temporal evolution of the Barombi Mbo Maar, a polygenetic maar-diatreme volcano of the Cameroon volcanic line. Int J Geosci 5:1315–1323. https:// doi.org/10.4236/ijg.2014.511108

3. Chako Tchamabé B, Ohba T, Kereszturi G, Németh K, Aka FT, Youmen D, Issa, Miyabuchi Y, Ooki S, Tanyileke G, Hell JV (2015) Towards the reconstruction of the shallow plumbing system of the Barombi Mbo Maar (Cameroon) Implications for diatreme growth processes of a polygenetic maar volcano. J Volcanol Geotherm Res 301:293–313. https://doi.org/10.1016/j.jvolgeores.2015.06.004

4. Chenet AL, Fluteau F, Courtillot V, Gérard M, Subbarao KV (2008) Determination of rapid Deccan eruptions across the Cretaceous-Tertiary boundary using paleomagnetic secular variation: Results from a 1200-m-thick section in the Mahabaleshwar escarpment. J Geophys Res 113:B04101. https://doi.org/10.1029/2006JB004635

5. Fisher RA (1953) Dispersion on a sphere. Proc R Soc Lond A 217:295–305. https://doi.org/10.1098/rspa.1953.0064

6. Freda C, Gaeta M, Karner DB, Marra F, Renne PR, Taddeucci J, Scarlato P, Christensen JN, Dallai L (2006) Eruptive history and petrologic evolution of the Albano multiple maar (Alban Hills, Central Italy). Bull Volcanol 68:567–591. https://doi.org/10.1007/s00445-005-0033-6

7. Giaccio B, Sposato A, Gaeta M, Marra F, Palladino DM, Taddeucci J, Barbieri M, Messina P, Rolfo MF (2007) Mid-distal occurrences of the Albano Maar pyroclastic deposits and their relevance for reassessing the eruptive scenarios of the most recent activity at the Colli Albani Volcanic District, Central Italy. Quat Int 171–172:160–178. https://doi.org/10.1016/j.quaint.2006.10.013

8. Graettinger AH, Valentine GA (2017) Evidence for the relative depths and energies of phreatomagmatic explosions recorded in tephra rings. Bull Volcanol 79:88. https://doi.org/10.1007/s00445-017-1177-x

9. Hatakeyama T (2013) Japan Archeomagnetism Database. http://mag.ifst.ous.ac.jp/en. Accessed Aug 2019.

10. Hatakeyama T (2018) Online plotting applications for paleomagnetic and rock magnetic data. Earth Planets Space 70:139. https://doi.org/10.1186/s40623-018-0906-5

11. Hyodo M, Itota C, Yaskawa K (1993) Geomagnetic secular variation reconstructed from magnetizations of wide-diameter cores of Holocene sediments in Japan. J Geomagn Geoelectr

45:669–696. https://doi.org/10.5636/jgg.45.669

12. Ishikawa T (1963) Topography and geology of the Daisetsu volcano group. Rep Nat Conserv Soc Jpn 8:5–24

13. Jarboe NA, Coe RS, Renne PR, Glen JMG, Mankinen EA (2008) Quickly erupted volcanic sections of the Steens Basalt, Columbia River Basalt Group: Secular variation, tectonic rotation, and the Steens Mountain reversal. Geochem Geophys Geosyst 9:Q11010. https://doi.org/10.1029/2008GC002067

14. Jordan SC, Cas RAF, Hayman PC (2013) The origin of a large (> 3 km) maar volcano by coalescence of multiple shallow craters: Lake Purrumbete maar, southeastern Australia. J Volcanol Geotherm Res 254:5–22. https://doi.org/10.1016/j.jvolgeores.2012.12.019

15. Kirschvink JL (1980) The least-squares line and plane and the analysis of palaeomagnetic data. Geophys J R Astron Soc 62:699–718. https://doi.org/10.1111/j.1365-246X.1980.tb02601.x

16. Konoya M, Matsui K, Kawachi S, Kobayashi T (1966) Geological map of Japan, Taisetsuzan (Abashiri-43). Hokkaido Development Agency, 1:50,000 geological map and explanatory text, p 47

17. Lorenz V (1973) On the formation of maars. Bull Volcanol 37:183–204. https://doi.org/10.1007/BF02597130

18. Lorenz V (2007) Syn- and posteruptive hazards of maar–diatreme volcanoes. J Volcanol Geotherm Res 159:285–312. https://doi.org/10.1016/j.jvolgeores.2006.02.015

19. Lucchi F (2019) On the use of unconformities in volcanic stratigraphy and mapping: Insights from the Aeolian Islands (southern Italy). J Volcanol Geotherm Res 385:3–26. https://doi.org/10.1016/j.jvolgeores.2019.01.014

20. McIntosh WC, Chapin CE, Ratté JC, Sutter JF (1992) Time-stratigraphic framework for the Eocene-Oligocene Mogollon-Datil volcanic field, southwest New Mexico. Geol Soc Am Bull 104:851–871. https://doi.org/10.1130/0016-7606(1992)104<0851:TSFFTE>2.3.CO;2

21. Moufti MR, Németh K, El-Masry N, Qaddah A (2013) Geoheritage values of one of the largest maar craters in the Arabian Peninsula: the Al Wahbah Crater and other volcanoes (Harrat Kishb, Saudi Arabia). Cent Eur J Geosci 5:254–271. https://doi.org/10.2478/s13533-012-0125-8

22. Németh K, Kereszturi G (2015) Monogenetic volcanism: personal views and discussion. Int J Earth Sci 104:2131–2146. https://doi.org/10.1007/s00531-015-1243-6

23. Ort MH, Lefebvre NS, Neal CA, McConnell VS, Wohletz KH (2018) Linking the Ukinrek 1977 maar-eruption observations to the tephra deposits: New insights into maar depositional processes. J Volcanol Geotherm Res 360:36–60. https://doi.org/10.1016/j.jvolgeores.2018.07.005

24. Pedrazzi D, Bolós X, Martí J (2014) Phreatomagmatic volcanism in complex hydrogeological environments: La Crosa de Sant Dalmai maar (Catalan Volcanic Zone, NE Spain). Geosphere 10:170–184. https://doi.org/10.1130/GES00959.1

25. Valentine GA, Cortés JA (2013) Time and space variations in magmatic and phreatomagmatic eruptive processes at Easy Chair (Lunar Crater Volcanic Field, Nevada, USA). Bull Volcanol 75:752. https://doi.org/10.1007/s00445-013-0752-z

26. Valentine GA, White JDL, Ross P-S, Graettinger AH, Sonder I (2017) Updates to concepts on phreatomagmatic maar-diatremes and their pyroclastic deposits. Front Earth Sci 5:68. https://doi.org/10.3389/feart.2017.00068

27. White JDL, Schmincke H-U (1999) Phreatomagmatic eruptive and depositional processes during the 1949 eruption on La Palma (Canary Islands). J Volcanol Geotherm Res 94:283–304. https://doi.org/10.1016/S0377-0273(99)00108-0

28. White JDL, Ross P-S (2011) Maar-diatreme volcanoes: A review. J Volcanol Geotherm Res 201:1–29. https://doi.org/10.1016/j.jvolgeores.2011.01.010

29. Yasuda Y, Sato E, Wada K, Suzuki-Kamata K (2015) Eruption interval between the two pyroclastic-flows from the Ohachidaira caldera of Taisetsu volcano, central Hokkaido, Japan: Estimation from the paleomagnetic directions. Bull Volcanol Soc Jpn 60:447–459. https://doi.org/10.18940/kazan.60.4_447

30. Yasuda Y, Suzuki-Kamata K (2018) The origin of a coarse lithic breccia in the 34 ka caldera-forming Sounkyo eruption, Taisetsu volcano group, central Hokkaido, Japan. J Volcanol Geotherm Res 357:287–305. https://doi.org/10.1016/j.jvolgeores.2018.04.017

31. Yasuda Y, Sato E, Suzuki-Kamata K (2020) Paleomagnetic constraints on a time-stratigraphic framework for the evolution of Ohachidaira volcano and the summit caldera, central Hokkaido, Japan. Bull Volcanol 82:71. https://doi.org/10.1007/s00445-020-01403-6

32. Zijderveld JDA (1967) A.C. demagnetization of rocks: analysis of results. In: Collinson DW, Creer KM, Runcorn SK (eds) Methods in palaeomagnetism, vol 3. Amsterdam, Elsevier, pp 254–286. https://doi.org/10.1016/B978-1-4832-2894-5.50049-5

Table 1

Table 1 is available in the Supplementary Files section.

Figures
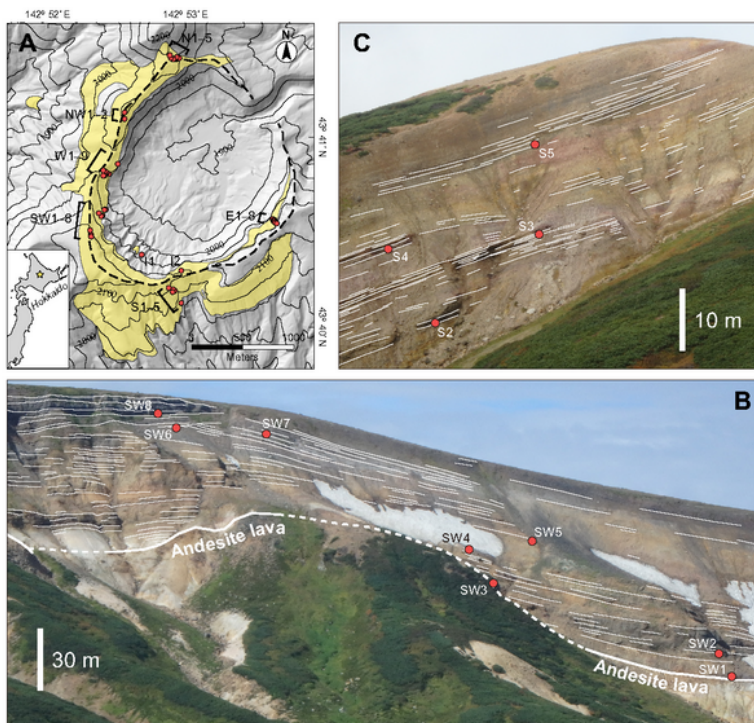
Figure 1

(A) Shaded relief map around Ohachidaira volcano, showing distribution of the Mamiyadake tephra ring (yellow). Red dots indicate sites sampled for paleomagnetic analysis. Dashed line delineates the caldera rim. Contour interval is 50 m. Inset map shows location of Ohachidaira volcano (yellow star). (B) Southwest wall of the Ohachidaira caldera. As much as 90 m of the tephra-ring deposits directly overlie older andesite lavas. Paleomagnetic directions here were determined at 8 sites (red dots; SW1–8). An

angular unconformity occurs between sites SW6−7 and SW8 (upper left). (C) West wall of the valley to the south of the caldera. Five sites (red dots; S1−5) were sampled for paleomagnetic analysis; the lowermost site (S1) is out of the photo to the lower left.
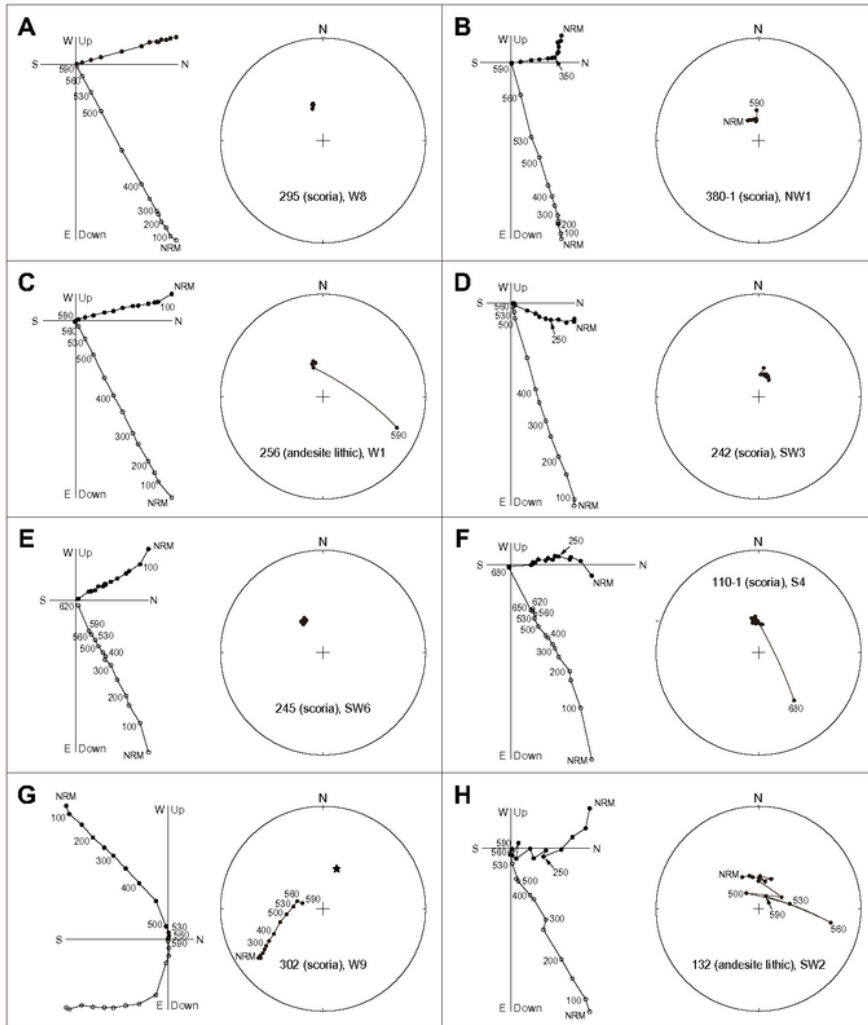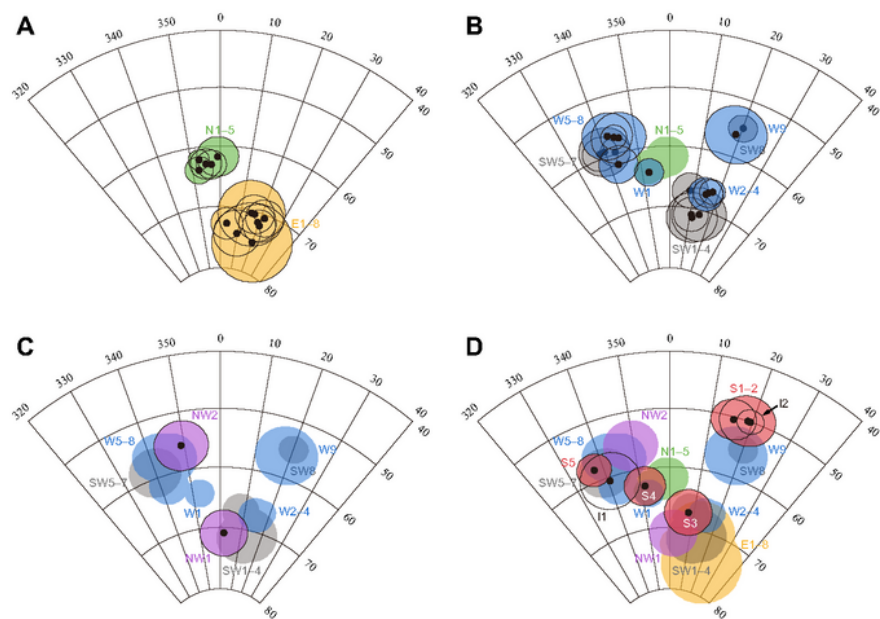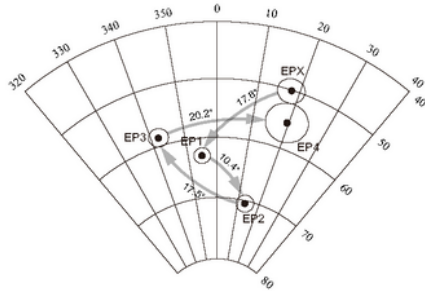

Figure 2

Orthogonal vector plots (left) and equal-area projections (right) of thermal demagnetization data for representative specimens. In orthogonal vector plots, open and solid dots represent projections on the vertical and horizontal planes, respectively. Numbers adjacent to data points indicate temperature in °C. (A−F) Specimens from which the characteristic remanent magnetization (ChRM) was successfully isolated during thermal demagnetization. (A) Specimen 295 (scoria) from site W8, showing a single stable component of magnetization. (B−F) After a low-temperature overprint is removed at 350 °C (B), 100 °C (C, E), or 250 °C (D, F), the ChRM decays linearly to the origin. (G) Specimen overprinted with a strong magnetization that was not removed even at the highest demagnetization step (590 °C). The star represents the mean ChRM direction of site W9. (H) Specimen rejected due to unstable demagnetization behavior even after removal of a low-temperature overprint at about 250 °C.

Figure 3

Equal-area lower hemisphere projections of site-mean directions for the Mamiyadake tephra ring. Dots represent site-mean directions and ellipses indicate 95% confidence circles (α_{95}). Colors are for clarity only. (A) The north (green, N1−5) and east (yellow, E1−8) sections. (B) The west (blue, W1−9) and southwest (gray, SW1−8) sections. Site-mean α_{95} ellipses for the north section are silhouetted. (C) The northwest section (purple, NW1−2). Site-mean α_{95} ellipses for the west and southwest sections are

silhouetted. (D) The south section (red, S1−5) and two isolated sites (open, I1−2). Site-mean α_{95} ellipses for all the other sections are silhouetted.

Figure 4

Equal-area lower hemisphere projection of the mean of site means for each eruptive episode (EP1−4, X). Dots represent episode-mean directions and ellipses indicate 95% confidence circles (α_{95}). Sites included

in each eruptive episode are identified in Table 1. Arrows indicate the shortest possible paths of paleosecular variation during formation of the Mamiyadake tephra ring. Angular distances between the mean directions are indicated beside the arrows. Eruptive episode X is tentatively placed ahead of eruptive episode 1 only to make the paths shortest.

Supplementary Files

This is a list of supplementary files associated with this preprint. Click to download.

- Table1.xlsx
- GraphicalAbstract.pdf
- TableS1.xlsx